Radio Science, Volume 36, Number 5, Pages 905–926, September/October 2001

Wavelet analysis of high-resolution temperature data with applications to radio wave scattering

C. Y. Chen and M. C. Kelley

School of Electrical and Computer Engineering, Cornell University, Ithaca, New York

D. L. Walters

Department of Physics, Naval Postgraduate School, Monterey, California

Abstract. High-resolution balloon-borne temperature measurements have been made in the troposphere and stratosphere during late fall over the western plains of the United States. In one such experiment the data are of remarkable quality and quite suitable for investigating methods of separating organized and turbulent features from a geophysical data stream, exploring atmospheric dynamics, and estimating VHF radar backscatter. We are particularly interested in the mechanisms creating aspect sensitivity, i.e., a nonunity ratio of vertical to well off-vertical radar backscatter. We find that very steep positive vertical temperature gradients, as high as 40.0 K/km, can be supported. On the other hand, negative gradients are limited to values near the marginal stability boundary. The structures are thus anisotropic and similar to ramp cliff features found in other fluids. We use wavelet analysis to isolate the organized components of the signal and, after subtraction, the residual signal is investigated to determine its character. The Fourier transform of the residual is Kolmogorov in nature, unlike that of the original data stream, and yields C_n^2, the refractive index structure parameter, in good agreement with the higher-order structure function approach; this supports the success of our partition. We calculate the Fresnel reflection coefficient using the wavelet coefficients; the turbulent scatter is found using C_n^2. The ratio between the Fresnel scatter and the turbulent scatter, i.e., the aspect sensitivity, is ~10 decibels in the troposphere and over 20 decibels in the stratosphere, in agreement with published observations and supporting our assumption that the organized features have horizontal extent exceeding the Fresnel scale.

1. Introduction

Radio waves are scattered in the lower atmosphere by variations in pressure, temperature, and humidity that produce variations in the refractive index [e.g., *Booker and Gordon*, 1950; *Bean and Dutton*, 1966; *Balsley and Gage*, 1980; *Balsley*, 1981]. It has been observed that at MF/HF/VHF frequencies, this radar backscatter is aspect sensitive; in other words, the ratio of the backscatter power in the vertical direction versus that in an off vertical direction is greater than unity [e.g., *Hooper and Thomas*, 1995; *Tsuda et al.*, 1997, and references therein]. It is generally thought that there are three scattering mechanisms creating this aspect sensitivity: Fresnel reflection, Fresnel scatter, and anisotropic turbulent scatter. Fresnel reflection, also termed partial specular reflection, is caused by vertical gradients of refractive index that are long lived and have horizontal dimensions larger in comparison to the first Fresnel zone. Scatters with horizontal dimensions less than the first Fresnel zone are known as Fresnel scatterers. On the other hand, turbulent structures with the scale size equal to one half of the transmitted wavelength can create echoes observable by high power radar systems such as the Arecibo Observatory (AO) and the Jicamarca Radio Observatory (JRO).

Paper number 2000RS002363.
0048-6604/01/2000RS002363$11.00

The Air Force Research Laboratory (AFRL) and the Naval Research Laboratory (NRL) have made a push toward high-resolution measurements of atmospheric temperature structures and turbulence for the purpose of characterizing the changes in atmospheric refractive index and their effects on a laser beam. Such a high-resolution balloon measurement of lower atmospheric temperature was taken at Wichita, Kansas on March 5, 1995. However, we can use this same in situ measurement to help us understand the atmospheric structures causing the aspect sensitive backscatter. In this paper, we will closely examine this high-resolution temperature data set.

We first present the instrument setup and the recorded data. Our attention is particularly focused on the sharp temperature gradients associated with potential temperature steps observed in the data. The potential temperature, the Brunt Väisälä frequency, and the gradient Richardson number reveal the atmospheric stability associated with the potential temperature steps. A Fourier analysis is then performed on the data set.

We believe the data have three components: localized, organized structures; turbulence; and instrument noise. We use wavelets to examine the validity of this proposal. Since wavelets can isolate features that are highly localized and have very high spatial frequency components, wavelet analysis is a more suitable analysis tool for data such as ours, which exhibit localized structures. We use wavelets to isolate the organized component of the signal and, after subtraction, the residual signal is investigated to determine its character. We also compute C_n^2 from the Fourier spectrum of the residual signal and compare it with the higher-order structure function approach. Once the edge dominant features are isolated, we show that the residual signal can be interpreted for evidence of quasi-homogenous turbulence [*Mallet and Zhong*, 1992; *Hagelberg and Gamage*, 1994; *Alcala et al.*, 2001].

We compute the backscattered signal the radar would measure from a series of layers formed by these sharp gradients, where the gradients are characterized by the wavelets. This initial wavelet-based scattering model assumes that the layers have a horizontal correlation length longer than that of the first Fresnel zone. Our approach is similar to that applied by *Alcala et al.* [this issue] and *Alcala and Kelley* [this issue] to the problem of polar mesosphere summer echoes (PMSE). We use the turbulent residual signal to calculate the turbulent backscatter by first computing the refractive index structure parameter C_n^2, a measure of refractive index fluctuations induced by the turbulence, which can be related to the radar volume reflectivity [*Panofsky*, 1968; *Balsley and Gage*, 1980; *Gage et al.*, 1980]. We compare the computed turbulent scatter to the calculated Fresnel scatter to determine the theoretical aspect sensitivity a 50 MHz radar may observe under the conditions given by the balloon sounding.

2. Experiment Background

2.1. Flight Conditions

The balloon launch occurred at 0100 LT on March 5, 1995 at Wichita, Kansas during the declining phase of a mild winter snowstorm. The sky was 100% overcast with light, dry snow up through the cloud top at the 1.3 km boundary layer inversion. The snow declined throughout the night and stopped by 0300 LT with clear conditions developing around sunrise. The surface temperature at launch was 0°C. Because of the light snow, there was some concern that ice could form on the probes, degrading operation or breaking the probes. This did not occur because of the very dry snow conditions and the cold temperature. Surface winds were light, ~1 m/s or less. The tropopause occurred at 10 km with relatively strong winds from the southwest at 30 m/s at 10 km and 12 km.

2.2. Instrumentation

The balloon payload consisted of two thermal turbulence sensors utilized in conjunction with a commercial VIZ 9000 microsonde system. The first was an uncoated 100 μm bead thermistor with 18 μm wire leads that had a temperature response time of 30 ms near the surface that increased to 90 ms in the stratosphere as the air density declined. The thermistor sampled every 1.25 s with an analog to digital converter resolution of 15-16 bits. This gave a temperature resolution of between 0.005-0.01 K. This relatively low-speed sensor provided absolute reference temperatures for the high-speed thermal turbulence sensor and larger-scale (>5 m) thermal turbulence data.

The high-speed thermal turbulence sensor was developed during 1994-1995 at the U.S. Naval Postgraduate School for the U.S. Air Force (USAF) Air-

borne Laser (ABL) program. It utilized a differential thermocouple pair with different thermal time constants DC coupled through an instrumentation amplifier and a 500 Hz analog bandpass filter. These fed a 12-bit analog to digital (A-D) converter operating at 310 samples per second. The digital serial bit stream fed a frequency shift keying (FSK) modulator that created a 130-150 kHz, amplitude-modulated subcarrier on the 304 MHz balloon telemetry signal.

The primary sensor in the thermocouple pair is a 12 μm thermocouple with a measured time constant of 5 ms at launch that increased to 15 ms in the stratosphere. The second thermocouple is constructed of a 24-gauge wire having a time constant of 10 s that increased to 30 s. The differential connection of the two thermocouples removed the common mean temperature while still responding to the turbulent thermal fluctuations. The differential operation of the high-speed temperature sensor suppressed the large-scale fluctuations that were handled by the independent bead thermistor.

Measurements of optical turbulence in the troposphere and stratosphere require a temperature resolution of 0.001-0.01 K. The 80 K temperature change from launch to the tropopause with a 0.001 K temperature resolution imposes a 17-bit dynamic range on the system. We handle this large temperature dynamic range by removing the large-scale fluctuation by the thermocouple and then oversampling the data at 310 Hz.

Wind speed was measured with a height resolution of 130 m via a LORAN (long-range navigation) system. Relative humidity information was not available.

3. Data Presentation

The low-resolution temperature data are presented in Figure 1 (left). The lapse rate in the troposphere is 7.1 K/km, less than the adiabatic lapse rate, whereas it is 0.53 K/km in the stratosphere. The tropopause is located at ~10 km. Even in the low-resolution data, considerable structure is evident in the temperature profile, a result upheld by the high-resolution measurement of the temperature fluctuation shown in Figure 1 (right). The data contain asymmetrical structures that are characterized by a sudden increase in temperature followed by a gradual decrease. These

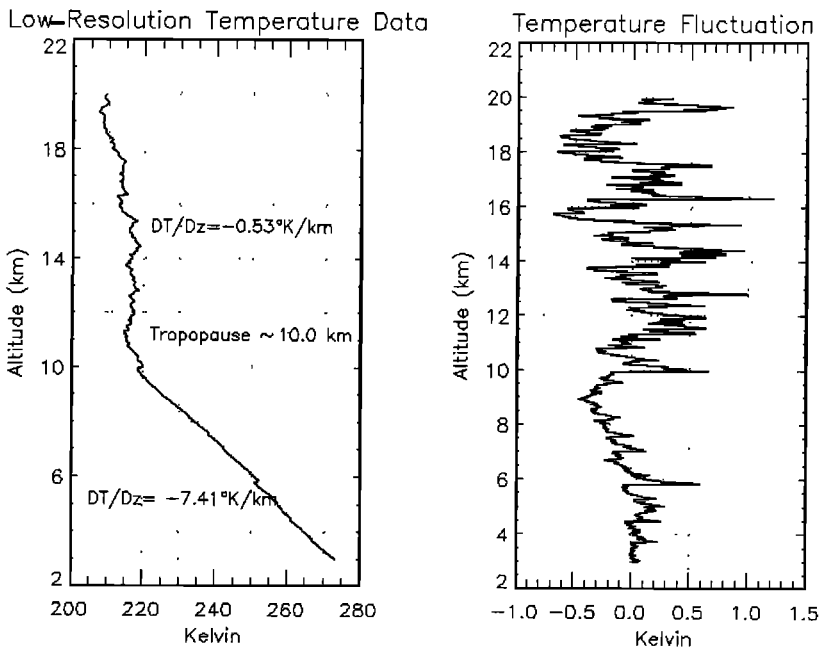

Figure 1. (left) Low-resolution temperature data as measured by a radiosonde over the skies of Wichita, Kansas on March 5, 1995. The tropopause is at ~10 km. (right) High-resolution temperature fluctuation. Asymmetrical structures, which are characterized by a sudden increase in temperature followed by a gradual decrease, are prevalent in the entire data set.

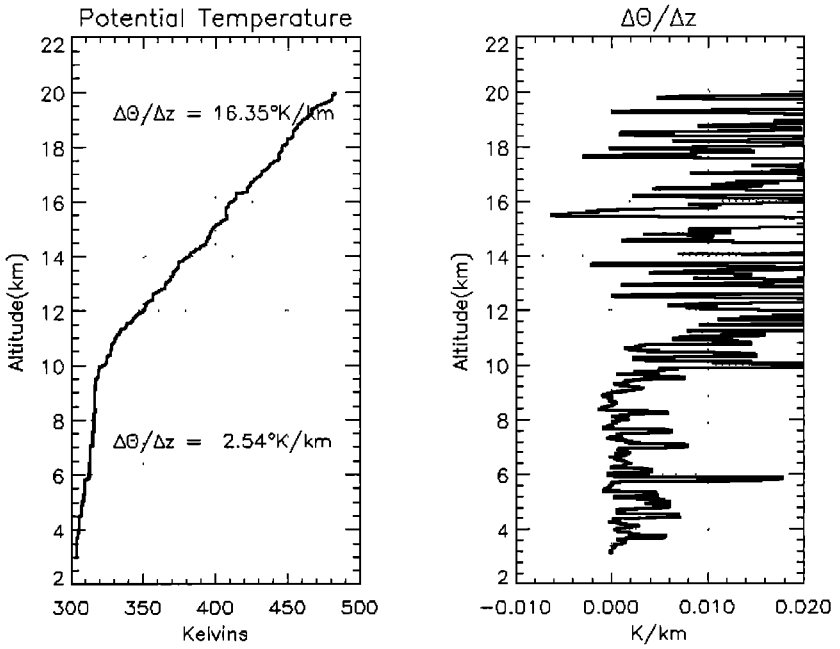

Figure 2. (left) Potential temperature. Many vertical potential temperature steps in the troposphere and the stratosphere. (right) Potential temperature gradient.

organized structures appear roughly every kilometer in the troposphere; similar structures are somewhat less obvious in the stratosphere but exist there as well. The positive temperature gradients are quite steep. Gradients as steep as 40 K/km are found in the stratosphere, while the steepest gradient in the troposphere is roughly one third of that value. On the other hand, the negative gradients are shallower, seldom dropping to less than −10 K/km. If isotropic turbulence does exist in our data set, and later we show that it may, it is overshadowed to the eye by anisotropic, large-scale structures.

In Figure 2, we plot the potential temperature (θ) along with its derivative. The potential temperature is defined in terms of temperature (T), pressure (p), the universal gas constant (R), the dry air specific heat at constant pressure, and a reference pressure (p_s), as

$$\theta = T(p_s/p)^{R/c_p} . \quad (1)$$

By definition, θ is the temperature that a parcel at pressure p would have when it is moved adiabatically to the reference pressure p_s, which we take to be 1000 mbar. We also see numerous examples of nearly vertical potential temperature steps. The anisotropic structures that we noticed in the temperature profile in Figure 1 correlate to the edges of the potential temperature steps. For this particular balloon sounding, these potential temperature steps are on the order of 100-1000 m thick in both the troposphere and the stratosphere.

The potential temperature gradient ($\Delta\theta/\Delta z$), plotted in Figure 2 (right), contains stability information about the atmosphere. The atmosphere is statically stable for positive values of the potential temperature gradient, unstable for negative values, and marginally stable when the gradient is zero [e.g., *Holton*, 1992]. We see that the average value of $\Delta\theta/\Delta z$ is ~2.54 K/km in the troposphere and ~16.35 K/km in the stratosphere. As expected, the tropopause forms the boundary between the slightly stable troposphere below and the very stable stratosphere above. The higher $\Delta\theta/\Delta z$ in the stratosphere corresponds to the higher stability of the region. In both regions of the atmosphere, $\Delta\theta/\Delta z$ sometimes becomes negative, indicating a parcel of heavier air overlying lighter air, creating an unstable situation. The center of the potential temperature steps, with $\Delta\theta/\Delta z \sim 0$, indicates marginally stable adiabatic parcels of air that are homogeneously mixed.

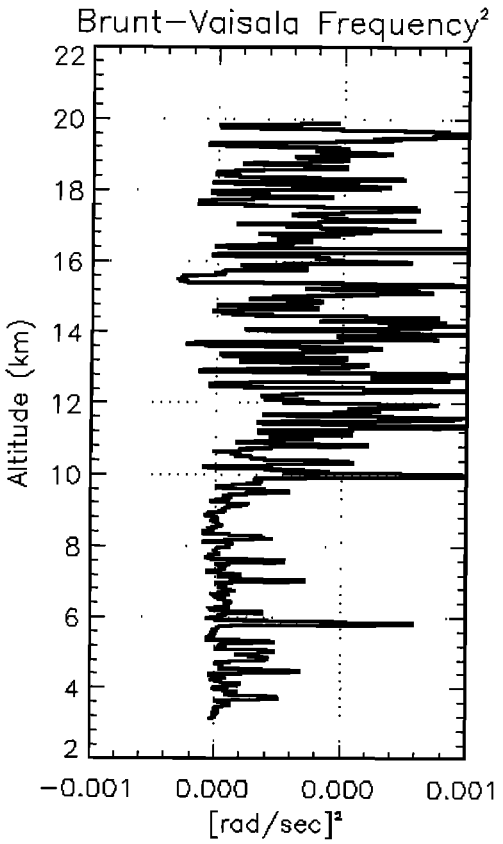

Figure 3. Square of the Brunt-Väisälä frequency. In the stratosphere, N^2=5.1×10^{-4} [rad/s]^2 and is N^2=7.13×10^{-5} [rad/s]^2 in the upper troposphere, which translates to a Brunt-Väisälä period of 4.64 min and 12.40 min, respectively.

This point is made clear in Figure 3, in which we calculate the square of the Brunt-Väisälä frequency,

$$N^2 = \frac{g}{\theta}\frac{d\theta}{dz}, \tag{2}$$

where g is gravity. This is another way of looking at the hydrostatic stability of the atmosphere. N^2 is a measure of the frequency of oscillation for a vertically displaced parcel of air. This oscillation is the result of the buoyancy force restoring the vertically displaced parcel back to its original location. If this parcel were in a highly stratified layer of atmosphere, the stratification would limit the vertical displacement of the parcel and increase the oscillation frequency. In other words, large positive values of N^2 imply a stably stratified atmosphere, while negative stability yields $N^2 < 0$. The average N^2 in the stratosphere is 5.1×10^{-4} [rad/s]^2 and is 7.13×10^{-5} [rad/s]^2 in the upper troposphere, which translates to a Brunt-Väisälä period of 4.64 min and 12.40 min, respectively. This again indicates the strong stability of the stratosphere and the marginal stability of the troposphere. Note that N^2 peaks near the edges of the temperature steps.

We display in Figure 4 the wind condition for this particular radiosonde sounding, with the wind magnitude in the left-hand panel and the wind direction in the right-hand panel. The wind was basically westward and steadily increased in speed up to the tropopause, remained steady near 25 m/s up to 15 km, and then decreased quickly with height. We can use this wind information in combination with the Brunt-Väisälä frequency to compute the gradient Richardson number,

$$Ri = \frac{N^2}{(dU/dz)^2}, \tag{3}$$

which is a measure of shear instability [*Bertin et al.*, 1997; *Werne and Fritts*, 1999, and references therein]. In this equation, U is the magnitude of the horizontal wind. Ri is a measurement of the ratio of the stabilization effect of the stratification, as signified by N^2, to the destabilization effect of the wind shear. We plot this in Figure 5. However, our measurement of the wind shear does not have a resolution as good as our temperature measurements and hence cannot give us a good indication of where shear instabilities occur. Nonetheless, on some occasions, it is clear that Ri is small in the regions where N^2 is near zero and/or the vertical shear is large and certainly is less than the stability boundary value of 0.25.

For a closer look at the asymmetrical structures seen in Figure 1 and to see how they tie in with potential temperature, we have magnified two of these asymmetrical structures. We also plot their associated potential temperature and N^2. The top row of Figure 6 shows an example in the troposphere where the sawtooth-like temperature fluctuations correlate to the edges of an almost vertical potential temperature step. Both $\Delta\theta/\Delta z$ and N^2 hover around zero near the center of the steps, implying a marginally stable condition where the air is very well mixed. We see a similar behavior in the stratosphere, as seen in the plots in the bottom row of Figure 6.

Passive temperature fluctuations which exhibit a characteristic structure (often termed ramps, triangu-

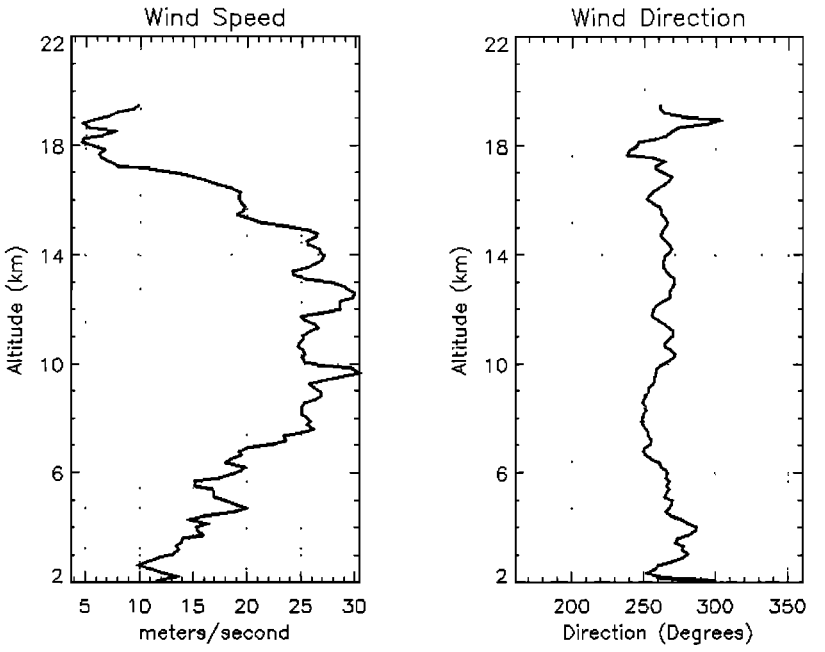

Figure 4. Wind profile measured on March 5, 1995. We see a westward wind with increasing velocity up to 10 km. The velocity is nearly constant between 10 km and 15 km and then decreases with height.

lar, or sawtooth patterns after their obvious geometrical signatures) have been observed in atmospheric turbulent shear flows, the ramps being effectively the signature of the large-scale structure of the flow [e.g., *Taylor*, 1958; *Antonia and Atkinson*, 1976; *Antonia et al.*, 1977; *Van Atta*, 1977]. The distinctive sawtooth feature is a result of large temperature jumps across sharp shear zones at the outer boundary of large-scale eddies. They also indicate that one important consequence of the ramp characteristic is the possible resulting anisotropy of small-scale scalar fluctuations [*Antonia et al.*, 1977]. *Kaimal and Businger* [1970] identified the ramp structure in the atmospheric boundary layer with individual convecting thermal plumes being sheared by the mean velocity gradient. On the other hand, the atmospheric temperature ramps may be interpreted as the signature of an organized large-scale motion rather than a necessary consequence of the presence of buoyant plumes [*Antonia et al.*, 1977]. In the propagation of optical and electrical magnetic radiation through the atmosphere these temperature ramps will account for a significant fraction of signal degradation [*Antonia et al.*, 1977].

Such anisotropic ramp structures have been reported earlier in the stratosphere and troposphere on the basis of the balloon data [*Barat*, 1982; *Barat and Bertin*, 1984; *Dalaudier et al.*, 1994]. In this context, the terms layers and sheets have been used to describe the temperature structure. *Bertin et al.* [1997] studied stratosphere sheet structures with high-resolution temperature and wind shear measurements and showed that low gradient Richardson numbers indeed occur in the regions of small negative potential temperature gradients, as we conjecture above.

However, according to work by *Werne and Fritts* [1999] and *Gibson-Wilde et al.* [2000] the vertical potential temperature steps are indicative of a dynamic instability, specifically, a Kelvin-Helmholtz (KH) type. KH instability is a shear instability. It initially begins as a small perturbation on a vertical shear where $Ri < 0.25$. As the instability develops, the amplitude of the motion increases and individual wave crests break, forming turbulent cores which concentrate the vorticity of the initial shear layer, forming the well-known cat's-eye pattern. As the turbulent energy decays, these billows become nearly horizontal stratified layers where the center of the

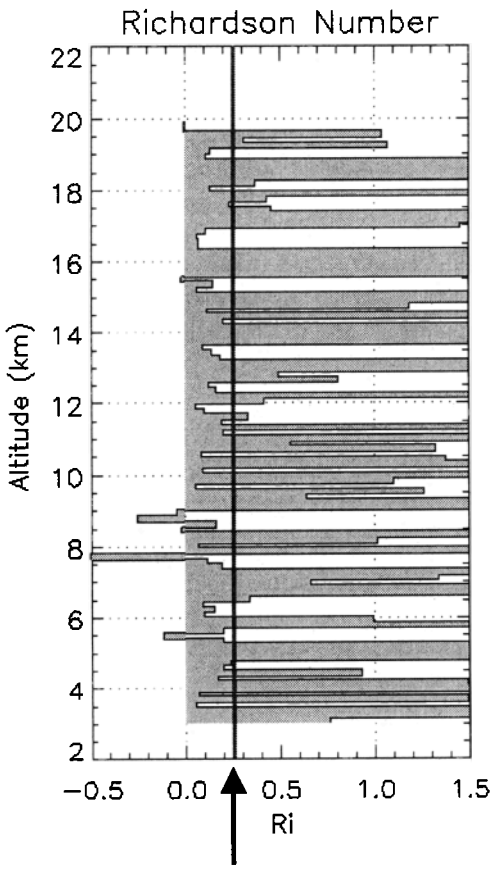

Figure 5. Gradient Richardson number (*Ri*). The resolution of this calculation is limited by the 130 m height resolution of the wind measurement. The arrow marks the line where $Ri = 0.25$, the marginally stable condition.

layer is marked by homogeneity, while the edges are indicated by sharp gradients. The results from *Werne and Fritts* [1999] are similar to those reported here.

4. Data Analysis

We turn to mathematical transforms in the hopes of understanding the atmospheric structures revealed by the in situ measurements. The popular Fourier analysis is first applied to the high-resolution temperature data. We also apply wavelet analysis to our data steam. There has been a great interest in using the recently developed wavelet transform technique for data analysis [e.g., *Alcala et al.*, this issue; *Alcala and Kelley*, this issue, and references therein]. Wavelets are able to analyze asymmetrical structures; hence it is reasonable to apply wavelet analysis to the temperature structures seen in Figures 1 and 6. We want to use the property of wavelets to parse the data into its components: the coherent atmospheric signal, turbulence, and instrument noise.

Before we begin our data analysis, however, we realize that the troposphere and the stratosphere can be looked upon as two fluids, the latter being more dynamically stable. This motivates us to parse the high-resolution data set at the tropopause (~10 km) into the stratosphere and the troposphere segments before we analyze the data set.

4.1. Fourier Analysis

We computed the Fourier spectrum of these high-resolution data and display the results in Figure 7. A least squares fit to a power law was performed on certain parts of the spectrum, the results of which are also illustrated in Figure 7. Note that these parts of the tropospheric and stratospheric sections both display a power law for the range $10^{-2} < k = 1/\lambda < 0.5$ with indices of –1.91 and –2.27, respectively. Both are considerably steeper than the –5/3-power law expected for isotropic turbulence in the inertial subrange [e.g., *Ottersten*, 1969b]. We see two dominant harmonics in both spectra at $\lambda = 2.5$ km and $\lambda = 1$ km. The 2.5 km component is a factor of two larger in magnitude in the stratosphere than in the troposphere.

A noise floor does not appear in either Fourier spectrum. It is quite possible for a signal to be greater than noise at all frequencies sampled. There is still the possibility that isotropic turbulence is present but too weak to be revealed by this type of analysis.

We believe that the result of the Fourier analysis is dominated by the large-scale, localized anisotropic structures, possibly with small-scale, isotropic turbulence and instrument noise superimposed. These anisotropic structures, we believe, caused the temperature spectrum to follow a steeper power law than the Kolmogorov –5/3 law. Hence, if we could isolate the localized components of our data, we might be able to separate them and search for the embedded isotropic turbulence, thereby enabling us to independently estimate radar backscatter from the edge and the turbulent component of the temperature profile. To do this, we turn to wavelets.

4.2. Wavelet Analysis

The wavelet transform is an integral transform localized in both space (time) and wave number (fre-

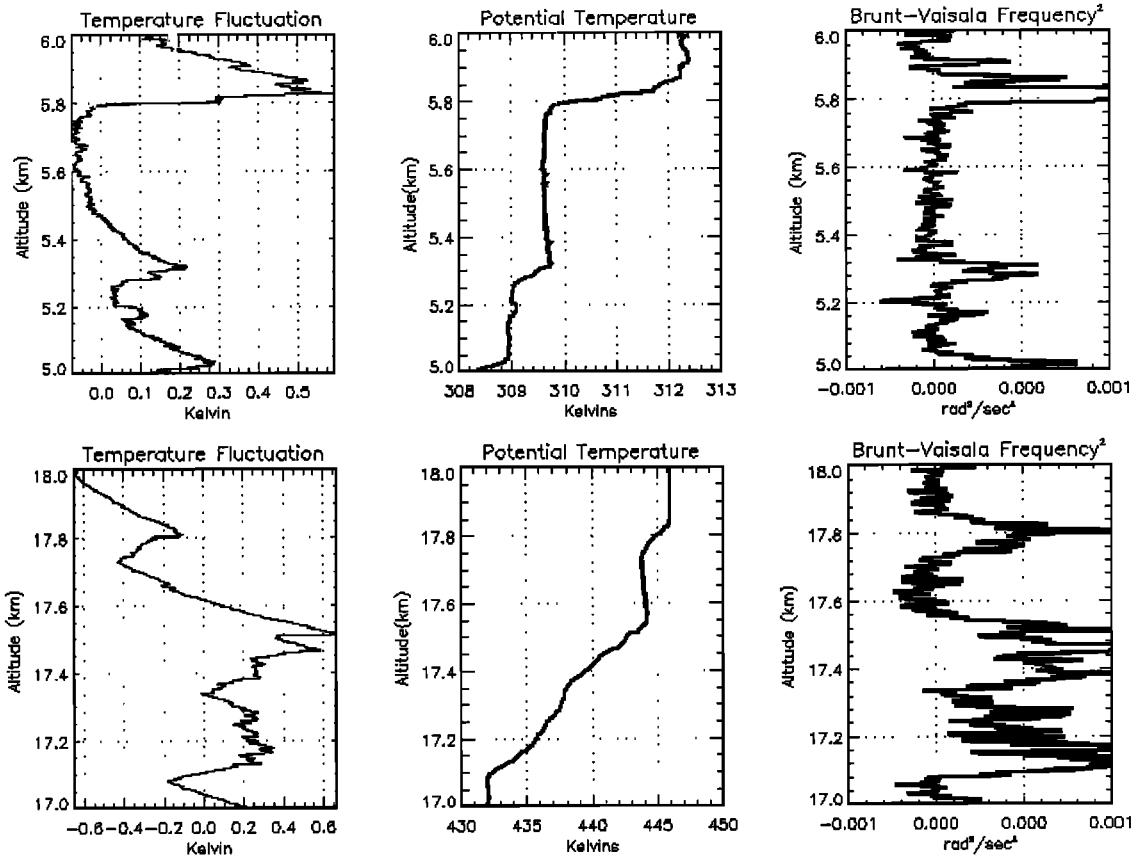

Figure 6. (top) An example of the temperature fluctuations observed in the troposphere. Plotted with it are the associated potential temperature and N^2. (bottom) A stratospheric example of the temperature fluctuation and the associated potential temperature and N^2.

quency). It differs from the Fourier transform in that instead of mapping the function of interest from space (time) to wave number (frequency), the wavelet transform maps the function from space (time) to space (time) and scale. In short, the wavelet transform divides the signal into different scale, analogous to different frequency, components and then studies each with a resolution to match its scale [*Daubechies*, 1992]. The transform thereby achieves the ability to locate and analyze short-lived, transient events such as the anisotropic structure in our atmospheric temperature measurement.

The basis function used gives the wavelet transform its time (space) and wave number (frequency) localization. We construct the basis functions by scaling and translating a reference function, i.e., a wavelet, $\psi(x)$ [*Kumar and Foufoula-Georgiou*, 1994; *Torrence and Compo*, 1998], forming

$$\psi_{\lambda,b}(x)=\frac{1}{\sqrt{\lambda}}\psi\left(\frac{x-b}{\lambda}\right). \tag{4}$$

The scale parameter λ dilates (or compresses) the wavelet, whereas b translates the wavelet. The wavelet transform of a function $f(x)$ is essentially the convolution of the wavelet with $f(x)$. For purposes shown later, the first derivative of a Gaussian, also known as the Canny edge detector, is our choice for a wavelet basis. It is defined as

$$\psi(x)=\left[-1/\sqrt{\Gamma(3/2)}\right]xe^{-x^2/2}. \tag{5}$$

The gamma function appears for normalization purposes [*Torrence and Compo*, 1998]. We illustrate in Figure 8 the behavior of the Canny edge detector in both the space and wave number domain. In formal

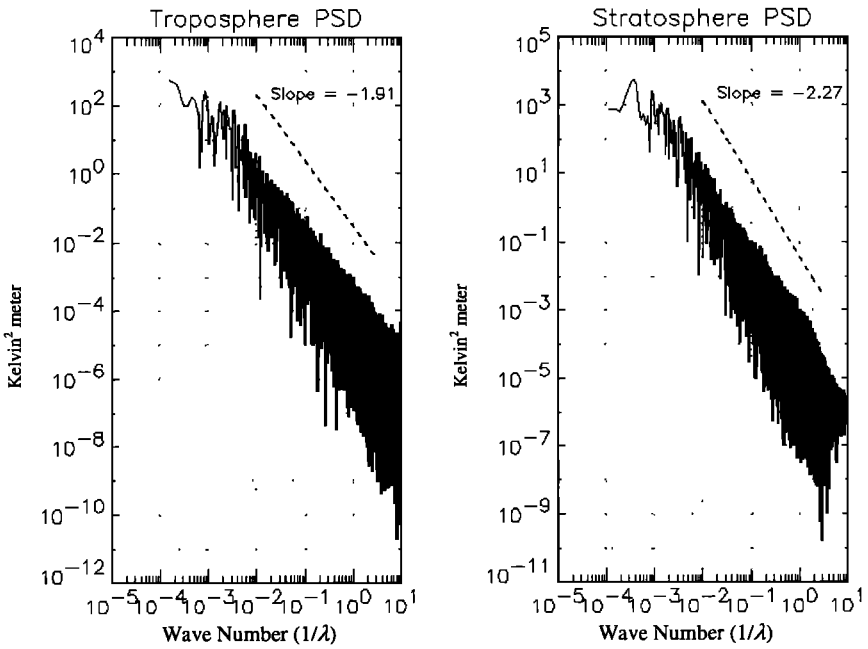

Figure 7. Fourier power spectrum of the tropospheric and stratospheric components of the data. We have performed a least squares fit to a power law to certain parts of the data. Both display power law for the range $10^{-2} < 1/\lambda < 0.5$ with indices of –1.91 and –2.27, respectively.

mathematical terms, the wavelet transform of a function $f(x)$ is defined as the integral transform

$$Wf(\lambda,x) = \int_{-\infty}^{\infty} f(u)\overline{\psi}_{\lambda,x}(u)du\,,\ \lambda > 0, \qquad (6)$$

where $\overline{\psi}_{\lambda,x}(u)$ is the complex conjugate of $\psi_{\lambda,x}(u)$. $Wf(\lambda, x)$ is the wavelet coefficient at λ. As we increase the scale λ, we dilate the wavelet so that the wavelet focuses in on the long-term behavior of $f(x)$ and vice versa [e.g., *Daubechies*, 1992; *Torrence and Compo*, 1998]. This property allows us to study the structure of the signal across different scales.

To demonstrate how wavelet decomposes the data, we have wavelet-transformed the temperature data and show an example of the result in Plate 1. Plate 1 (bottom panel) shows the normalized wavelet scalogram of a detrended temperature data from z = 3.6 km to 4.0 km. The normalized scalogram, which displays the normalized wavelet coefficient at each λ, shows us the partitioning of signal energy between the various scale sizes. It allows us to visually track features in the data from large to small scales. The scalogram also preserves the sign of the amplitude because of the asymmetry of the analyzing wavelet. By comparing the scalogram with the original data we see that positive coefficients, denoted by red, describe a negative gradient in the temperature profile.

We can identify several different types of features in the temperature data from the scalogram. The main feature is the strong gradient just above 3.7 km. The strong gradient, or edge, is part of a sawtooth-shaped anisotropic temperature structure. The gradient contains structures in the large scale of the order of tens of meters down to scales comparable to the VHF Bragg wavelength. Only large-scale structures are detected from the downward sloped portion of the temperature structure. The data also contain several other strong features that maintain their coherency over multiple scale sizes, such as the ones near 3.68 km and 3.83 km. We suspect that these structures are responsible for the Fresnel reflection component of the radar backscatter. Moreover, weaker high-frequency oscillations ("fuzz"-shaped structures) exist throughout the data stream. These weaker structures typically have structure only at scales smaller than a few meters. They also tend to be homogeneously distributed throughout the data, suggesting the presence of a nonlocal phenomenon such as instrument noise or atmospheric turbulence.

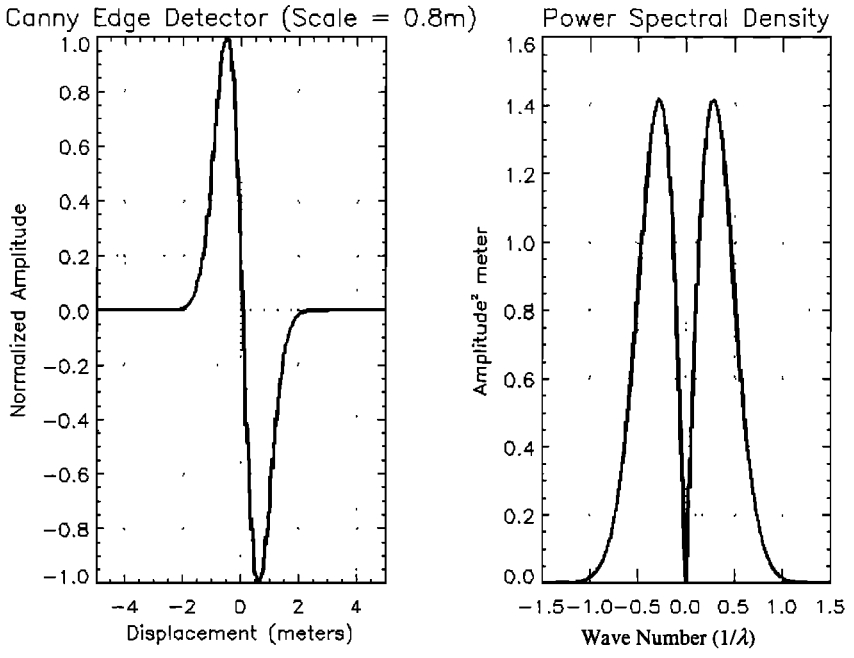

Figure 8. Time series of the Canny edge detector and its Fourier power spectrum.

4.3. Edge Tracking

We want to extract information about the edges and turbulence in the data to determine their contribution to the scattered power received by a radar. The temperature gradient at 3.7 km is a clear example of an edge component. In contrast, turbulent mixing is a statistical process where different eddies appear and disappear randomly over some volume and have homogeneous properties over the range of the data considered. To do this, we need to separate the two components in the signal, relying on the fact that the edge components are coherent structures with localized structures persisting over multiple scale sizes. In other words, we can isolate the edges by requiring that wavelet coefficients must track down from the larger scales. Using this method, we will be able to separate the coherent from the turbulent component of the data set. This method of signal processing forms the basis for several data compression and noise suppression algorithms [*Mallat and Zhong*, 1992; *Saito*, 1994]. In addition, *Hagelberg and Gamage* [1994] use a similar technique to detect coherent structures in velocity and temperature measurements in the atmospheric boundary layer during turbulent events. *Alcala et al.* [this issue] and *Alcala and Kelley* [this issue] applied a similar technique to remove the instrument noise from an in situ electron density measured in a PMSE event.

As an example, we apply this edge-tracking algorithm to the tropospheric section of data examined in Plate 1. We plot the original data in the top panel and the reconstructed data via edge coefficients in the second panel. We obtain the contribution of the turbulence and noise by subtracting the reconstructed data from the original data. As Plate 1 clearly illustrates, the edge-tracking algorithm is able to remove the fuzz-like component from the data. We suspect that turbulence is the cause for this fuzz; as we will show later, this is substantiated with a Fourier analysis result. Plate 2 shows the result of the edge-tracking algorithm applied to a portion of the data in the stratosphere.

Satisfied with the wavelet analysis results thus far, we proceed to apply the edge-tracking algorithm to the entire tropospheric and stratospheric data sets and to plot the Fourier power spectra of the turbulence residuals from the data set in Figure 9. Both spectra follow a power law near the predicted by Kolmogorov's theory for isotropic turbulence. We believe this result is evidence for a background turbulent atmosphere. There are indications for a noise floor, particularly for $1/\lambda > 0.1$, indicating a limitation in the instrument resolution.

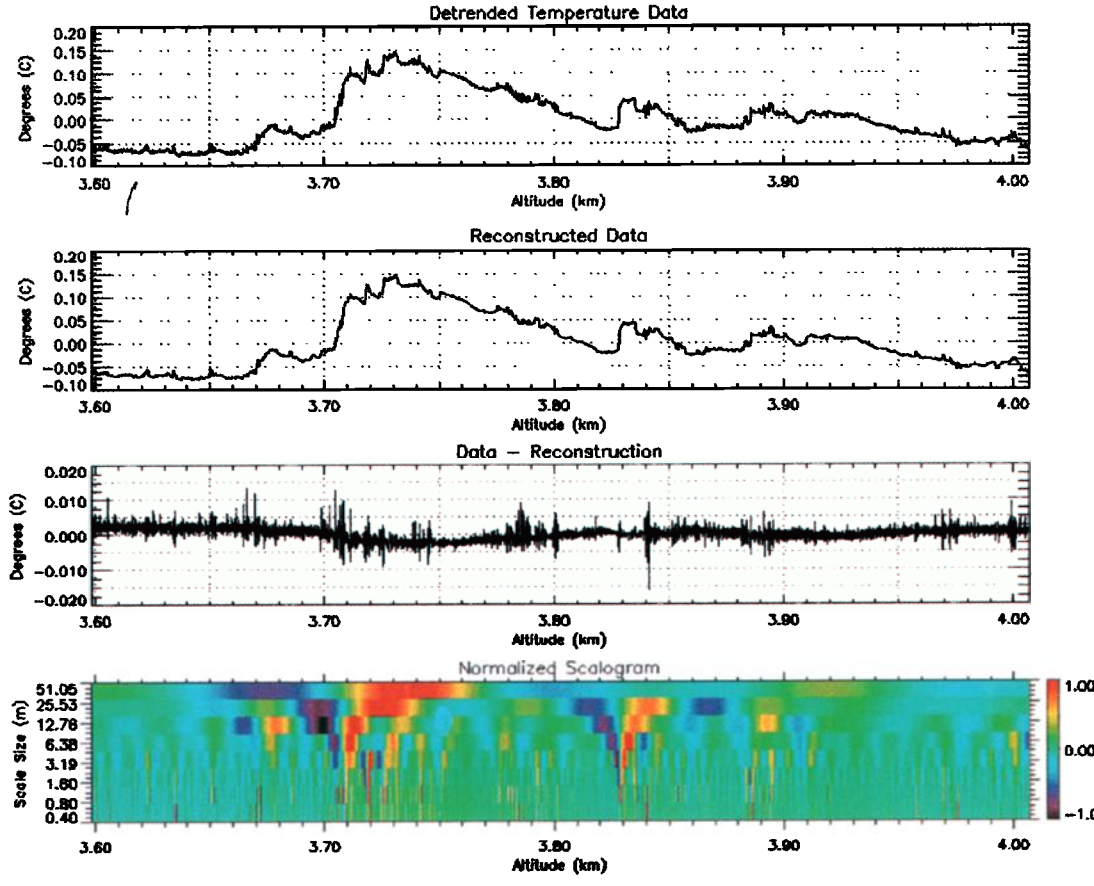

Plate 1. A sample result of our wavelet analysis performed on a piece of data. Our wavelet analysis involves not only wavelet transforming the data set and computing a scalogram, but also the edge-tracking algorithm, which isolates the coherent structures in the data from noise and/or turbulence. We show the detrended original data in the top panel and the reconstructed data in the second panel. The difference between the original data and the reconstituted data is in the third panel, and we plot the scalogram of the data in the fourth panel.

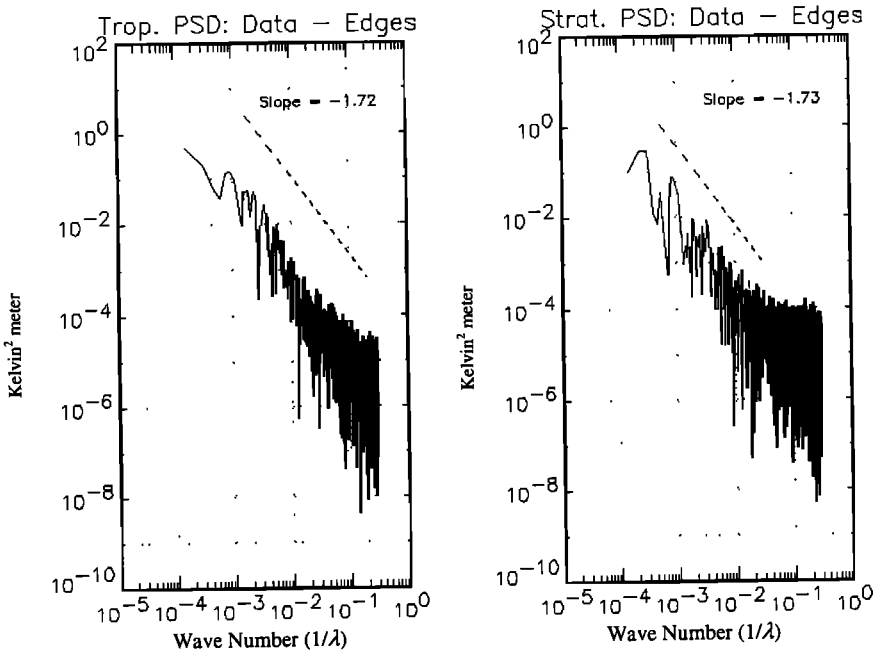

Figure 9. Fourier power spectrum of the tropospheric and stratospheric component of the residue removed from the original data by the edge-tracking algorithm. Note that both power spectra are consistent with a –5/3 power law of the Kolmogorov isotropic turbulence theory.

Further evidence for the existence of a turbulent component is provided in section 6, where we calculate C_n^2 from both the Fourier transform of the turbulence residual and the higher-order structure function.

5. Fresnel Reflection From Horizontally Stratified Media

The next goal of this paper is to calculate and compare the turbulent and edge components of the radar backscatter that a radar could generate under the conditions of the balloon temperature sounding. Now that we have parsed the data into edge and turbulent components, we want to develop a model that can compute the reflection coefficient for a given edge.

We can determine the magnitude of the electric field reflected from a scattering layer with a refractive index greater than unity. Defining ρ as the ratio of the reflected electric field to the incident field, *Wait* [1962] gives ρ from a horizontally stratified layer obtained from the generalized WKB solution,

$$\rho = \frac{1}{2}\int_{z2}^{z1}\left[\frac{1}{n}\frac{d}{dz}n\right]e^{-2jk_0 z}dz\,, \qquad (7)$$

where $k_0 = 2\pi/\lambda$ and λ is the radar wavelength. For the lower atmosphere the refractive index depends on a combination of water vapor and density fluctuations [*Balsley and Gage*, 1980].

It is important to use a smooth function to represent the discontinuities in the refractive index. *Alcala et al.* [this issue] showed that the discontinuities in $n(z)$ can overestimate the backscatter power. Our wavelet basis functions satisfy this smoothness requirement. In addition, our model assumes that all reflections are Fresnel reflections. In other words, the layers causing the reflection have a horizontal extent larger than the first Fresnel zone.

We model the refractive index fluctuations specified by the derivative of a Gaussian, first proposed by *Hocking* [1987] and then used by *Alcala and Kelley* [this issue], for calculating theoretical PMSE echoes, given a rocket sounding electron density profile. Following *Alcala and Kelley* [this issue], we assume that the index of refraction is defined as

$$n(z) = 1 + \Delta n(z), \qquad (8)$$

where $\Delta n(z) << 1$. We model $\Delta n(z)$ as a wavelet. In other words, we define an index fluctuation centered

at an altitude z_o at a scale size h as

$$\Delta n = n_o \sqrt{h} \frac{d}{dz} e^{-(z-z_o)^2/4h^2} = -n_o \frac{1}{\sqrt{h}} \left(\frac{z-z_o}{2h} \right) e^{-(z-z_o)^2/4h^2} \quad (9)$$

with the reflection coefficient

$$\rho(z_o) \approx -4\sqrt{\pi}(k_o h)^2 \left(\frac{n_o}{\sqrt{h}} \right) e^{-(d_o/2\sigma_r)^2} e^{-4k_o^2 h^2} e^{-2jk_o z_o}, \quad (10)$$

where n_o is the amplitude of a refractive index fluctuation as modeled by a wavelet, d_o is the distance between z_o and the center of a range gate, and σ_o is the full width at half-max of the antenna pattern. We have tacitly assumed that $\Delta n(z)$ has a infinite horizontal correlation length. Modeling $\Delta n(z)$ as a wavelet allows us the convenience of using the wavelet coefficients to calculate the Fresnel scattering as dictated by the in situ temperature profile.

Via the Born approximation, we can apply (10) to scattering from multiple layers in a given range gate. The total refractive index fluctuation of N layers is simply the sum of the fluctuation from each layer. Extending this concept to reflection coefficients, the total reflection coefficient from N layers is

$$\rho_{\text{total}} = \sum_{i=0}^{N-1} \rho_i(z_{oi}), \quad (11)$$

where ρ_i is the reflection coefficient caused by layer i centered at z_{oi}. The summation arises because the reflection coefficient, and therefore the reflected electric field, is a linear function of the refractive index fluctuations.

We show the calculated square of the magnitude of the reflection coefficient versus altitude for our in situ temperature profile and the Canny edge detector using the dashed curve in Figure 10. To do this, we isolate a segment of data equivalent to the vertical depth of the radar range gate. The edge-tracking algorithm then gives us the location of the edges as well as the associated wavelet coefficients which, via (9), (10), and (11), give us ρ_{total}. In this calculation, we assume that our radar is operating at 50 MHz and a range resolution of 300 m, parameters typical for a

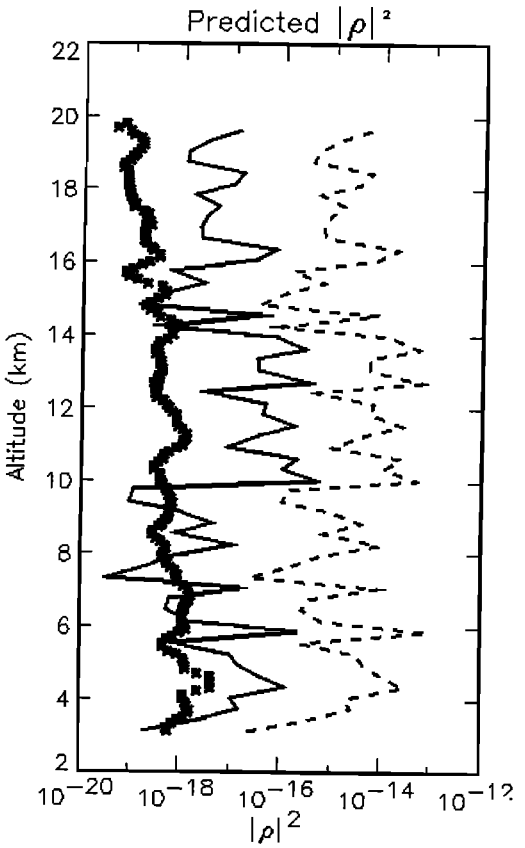

Figure 10. The predicted $|\rho|^2$ that a radar may observe in the atmospheric condition described by the temperature profile in Figure 1. Dashed curve is $|\rho|^2$ predicted from our wavelet model of a refractive index perturbation assuming an infinite horizontal correlation length. Solid curve is $|\rho|^2$ predicted from our wavelet model of a refractive index perturbation assuming a finite horizontal correlation length computed from the observation in *Sato et al.* [1985]. Starred curve is the predicted $|\rho|^2$ from isotropic turbulence.

VHF radar such as the middle and upper atmosphere (MU) radar and the Jicamarca Radio Observatory (JRO). Furthermore, we make the dry air approximation, as the relative humidity data are not available; gradients in the relative humidity will affect the index of refraction and hence the radar backscatter [*Balsley*, 1981].

Information on the horizontal correlation length of the scatterer improves our reflection coefficient prediction. We can compute the horizontal correlation length from the aspect sensitivity echoes. *Sato et al.* [1985] made aspect sensitivity measurements at the MU radar which yielded an aspect sensitivity of ~5

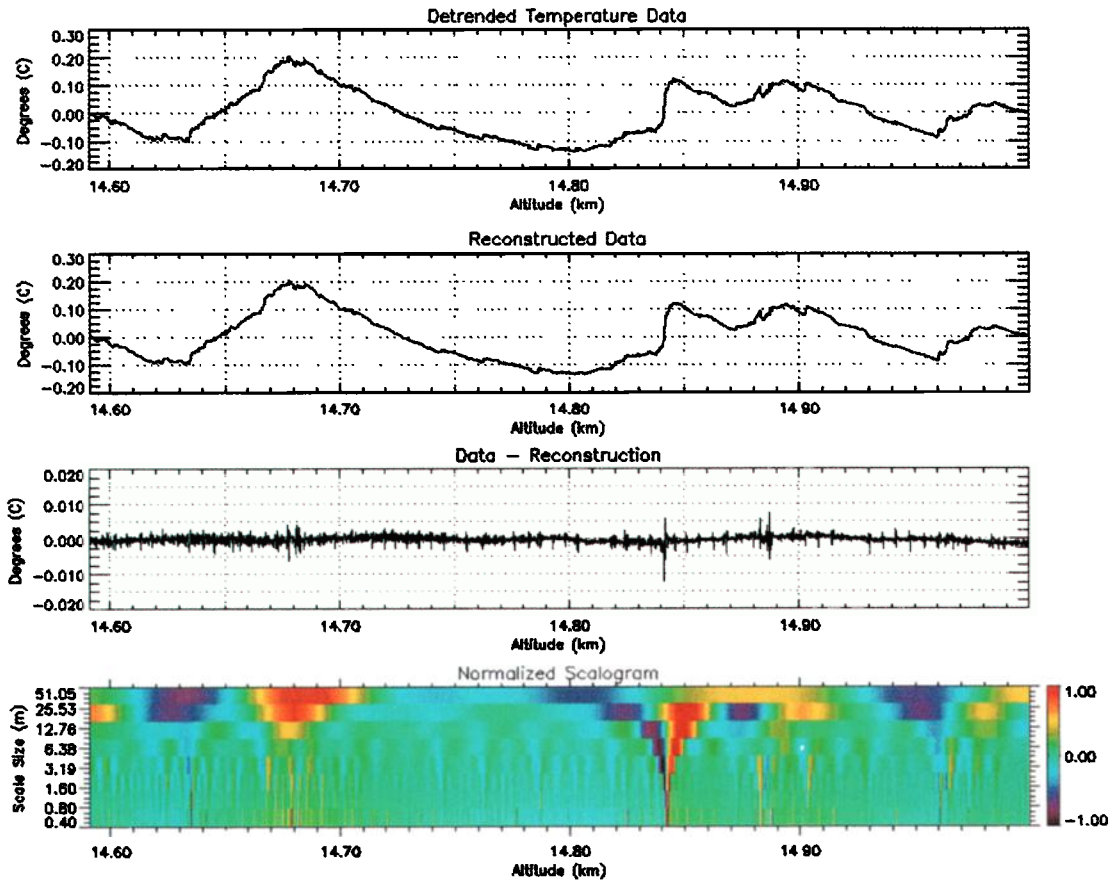

Plate 2. Wavelet analysis performed on a sample stratospheric component of our data. This plot follows the same format as in Plate 1.

decibels in the troposphere and ~15 decibels in the stratosphere. To compute the horizontal correlation length from the aspect sensitivity, we first need to compute θ_S, which is a more general parameter that quantifies the degree of aspect sensitivity described by *Hooper and Thomas* [1995] and *Hocking et al.* [1986, 1990]. θ_S for a truly specular reflector approaches 0°, whereas for isotropic scatterers θ_S approaches infinity; in practice, any value in excess of ~20° can be regarded as almost isotropic. We compute θ_S by first assuming that a scatterer at any particular height has a backscatter polar diagram of the type

$$\exp\left(-\theta^2/\theta_S^2\right). \tag{12}$$

θ_S is then determined by comparing the backscatter power, $P(\theta)$, received for two zenith angles θ_1 and θ_2:

$$\theta_S = \sqrt{\frac{\theta_2^2 - \theta_1^2}{\ln[P(\theta_1)/P(\theta_2)]} - \theta_0^2}\,, \tag{13}$$

where θ_0 is the half-power half width of the radar beam. For the experiment described by *Sato et al.* [1985], $\theta_0 = 2°$, $\theta_1 = 0°$, and $\theta_2 = 15°$. This gives us $\theta_S = 13.5°$ for the troposphere and $\theta_S = 7.2°$ for the stratosphere. With an additional assumption that the scatterer is an ellipsoid with a vertical depth of $h \approx 0.2\lambda$, one can show that the horizontal correlation length is given by [*Hocking et al.*, 1986]

$$\zeta = 0.13\lambda/\sin\theta_S. \tag{14}$$

For the MU radar, $\zeta \sim 3$ m in the troposphere and $\zeta \sim 5.6$ m in the stratosphere.

Alcala and Kelley [this issue] derived an expression comparing $|\rho|^2$ from a scatterer of finite horizontal correlation length with scatterer of an infinite horizontal correlation length. The ratio is

$$\frac{|\rho(\zeta)|^2}{|\rho(\infty)|^2} = \left[\frac{8k_0A^2h^2}{\sqrt{z^2 + 64k_0^2A^4h^4}}\right]^2, \tag{15}$$

where $k_0 = 2\pi/\lambda$, $A = \zeta/h$, z is the range to the scatterer, and $h \approx 0.2\lambda$ is the vertical scale length of the most effective backscatter [*Briggs and Vincent*, 1973]. As a consistency check, we see that as ζ increases, the ratio of $|\rho|^2$ approaches unity. We will use this result to improve our scattering calculation so that it accounts for the horizontal correlation length of the scatterer as determined from the aspect sensitivity measurement. We then define a "corrected" $|\rho|^2$ as

$$|\rho|^2_{\text{corrected}} = \frac{|\rho(\zeta)|^2}{|\rho(\infty)|^2}\,|\rho|^2_{\text{original}}, \tag{16}$$

where $|\rho|^2_{\text{original}}$ is the $|\rho|^2$ computed for a scatterer with an infinite horizontal correlation length. Our result is plotted as the solid curve in Figure 10. We see that the assumption of the infinite horizontal extent of the scatterer can lead to an overestimate of radar backscatter by an order of magnitude. The starred curve is discussed below.

VHF radars have been used to measure the Fresnel reflection coefficient in the troposphere the lower stratosphere [e.g., *Green and Gage*, 1980; *Dalaudier et al.*, 1989, 1994]. Our calculated reflection coefficient profile compares well with the measured results.

6. Radar Scatter From Turbulence

The radar backscatter from isotropic turbulence depends on C_n^2, a measure of refractive index fluctuations induced by the turbulence. We can calculate C_n^2 via one of two ways. C_n^2 can be determined from a high-order structure function as defined by a higher-order difference, an esoteric method to calculate C_n^2 that has been verified experimentally [*Walters*, 1995]. C_n^2 can also be formed from the Fourier spectrum of a turbulence-affected passive scalar, e.g., temperature. Hence, in this second method, we calculate C_n^2 by Fourier transforming the turbulent component of the temperature data set as isolated by the edge-tracking algorithm. This method is new. We want to compare the C_n^2 calculated using the two methods as a verification of the ability of the edge-tracking algorithm to parse the data into the edge and turbulent components. This result will then be applied to a radar scattering calculation.

6.1. Calculation of C_n^2 Using the Structure Function

Over the past two decades, balloon-borne microthermal probes have collected high-resolution atmospheric C_n^2 profiles. The measurement method involves launching meteorological balloons equipped with sensors that measure the microstructure of the thermal field during the free flight ascent from

ground level up to ~25-30 km [e.g., *Bufton et al.*, 1972; *Coulman et al.*, 1995; *Walters*, 1995]. Typically, the C_n^2 data come from temperature differences measured by fluctuations in the resistance of two fine-wire platinum or tungsten probes separated horizontally by ~1 m.

The theoretical basis of such a measurement originates from the Kolmogorov structure function. An nth order structure function is defined as the mean of the nth power of the difference of the values of a variable at the distance r apart [e.g., *Panofsky*, 1968]. More specifically, the conventional structure function D_X^n is of the form

$$D_X^n(\mathbf{r}_1, \mathbf{r}_2) = \langle [X(\mathbf{r}_1) - X(\mathbf{r}_2)]^n \rangle, \tag{17}$$

where X is an atmospheric scalar parameter such as the temperature or index of refraction, $\mathbf{r}_1$ and $\mathbf{r}_2$ are position vectors of two points in space, and the angled brackets imply an ensemble average. Equation (17) may follow a power law, allowing one to write

$$D_X^n(|\mathbf{r}_2 - \mathbf{r}_1|) = C_X^n r^m, \tag{18}$$

where

$$|\mathbf{r}_2 - \mathbf{r}_1| = r \tag{19}$$

and $0 < m \leq 2$. The structure parameter C_X^n is a proportionality constant. The second-order Kolmogorov structure function has been used for turbulence study. Over sufficiently small regions, of the order of millimeters to meters in size, for which the turbulence is locally homogeneous and isotropic, the atmosphere can have just such a Kolmogorov structure function dependence with $m = 2/3$. The turbulence sensor examines temperature, a scalar parameter, via $D_T(r)$ by measuring the root-mean-square (RMS) temperature difference between two thermometers separated by 1 m; in other words, $r = 1$. Within these constraints, a passive additive such as the atmospheric index of refraction structure parameter becomes [*Tatarskii*, 1961; *Doviak and Zrnic*, 1984]

$$C_T^2 = \frac{\left\langle [T(\mathrm{r}_2) - T(\mathrm{r}_1)]^2 \right\rangle}{r^{2/3}}. \tag{20}$$

C_T^2 is the temperature structure function coefficient. We relate C_T^2 to C_n^2, the refractive index structure function coefficient, via the pressure and temperature measurement with the standard formula [e.g., *Coulman et al.*, 1995]

$$C_n^2 = \left(7.9\times10^{-5}\frac{P}{T^2}\Gamma\right)^2 C_T^2. \tag{21}$$

Humidity affects the relationship between C_T^2 and C_n^2 via Γ, which is unity for dry air. In our analysis, since we do not have relative humidity information, we will use the dry air approximation. In short, an in situ instrument can provide us the atmospheric C_T^2; however, C_n^2 is the relevant parameter needed to compute backscattered power.

However, one can also compute C_n^2 directly and indirectly from atmospheric temperature measurements. One can compute C_n^2 from a higher-order structure function as defined by a higher-order difference, a more esoteric method. This has been verified experimentally by *Walters* [1995]. C_n^2 is also proportional to the Fourier spectrum of a turbulence-affected passive scalar, e.g., temperature. Hence, in this second method, we calculate C_n^2 by Fourier transforming the turbulent component of the temperature data set as isolated by the edge-tracking algorithm. The relationship between C_n^2 and the Fourier spectrum of a turbulent scalar parameter was developed in the late 1960s [e.g., *Ottersten*, 1969a, 1969b]; using wavelet analysis as part of this process is new. We examine the C_n^2 computed from these two methods. As an application, we will use C_n^2 to calculate a theoretical turbulence backscatter that a radar may experience given the atmospheric condition as specified by the temperature sounding and relate this to observations of aspect sensitivity.

6.2. Calculation of C_T^2 Using the Higher-Order Structure Function

Collecting C_T^2 profiles with multiple microthermal probe pairs carried by a balloon tends to be awkward and expensive. To simplify the atmospheric C_T^2 vertical profile measurement, *Walters* [1995] investigated the use of vertical temperature differences obtained from a vertical sequence of data collected from a single temperature probe carried by a balloon. To circumvent large amplitude, low-frequency trends in the vertical temperature data, the data reduction procedure involved using the pth-order differences of a random process on the temperature measurements [*Yaglom*, 1987]. This combination of a single probe with the pth-order difference provides results that are equivalent to those collected with conventional, hori-

zontal differential temperature probes [*Walters*, 1995].

Yaglom [1987] introduced the generalized structure functions for pth order, stationary random processes in terms of the pth-order differences. In other words, a pth-order, self-similar, stationary random process $X(r)$ has a pth-order difference expressed as

$$\Delta_r^p X(\rho) = \sum_{k=0}^{p} (-1)^k \binom{p}{k} X(\rho - kr). \qquad (22)$$

Following *Walters* [1995] and *Yaglom* [1987], the mean square of (22) gives the pth-order structure function

$$\left\langle \left| \Delta_r^p X(\rho) \right|^2 \right\rangle = D^{(p)}(r). \qquad (23)$$

$D^{(p)}(r)$ is a pth-order structure function having the form

$$D^{(p)}(r) = C^{(p)} |r|^m, \qquad (24)$$

where r is as defined in (19) and $C^{(p)}$ is the pth-order structure parameter. For turbulence applications, m = 2/3. Equation (24) is analogous to the conventional Kolmogorov structure function, as seen in (17).

Walters [1995] shows that one can relate $C^{(p)}$ to C_T^2 by

$$C^{(p)} = C_T^2 \sum_{j=0}^{p-1} \binom{2p}{j} (-1)^{p+1} (p-j)^m . \qquad (25)$$

The structure parameter for the first-order difference is equal to C_T^2, while for higher-order differences the structure parameter $C^{(p)}$ is directly proportional to C_T^2. In other words, for atmospheric vertical temperature data we can use (22) to remove the large-scale, inhomogeneous components of the temperature data, computing C_T^2 via (25) and C_n^2 via (21).

We have computed the first- and second-order structure parameter of the temperature data in Figure 11. The sums are carried out over the entire data set while setting r = 1 m and then averaging the result over 5 m before plotting. As was also found by *Walters* [1995], C_n^2 calculated from the first-order vertical temperature difference as defined by (12) overestimates C_n^2 by two orders of magnitude. We show this as the dashed curve. The structure parameter from the second-order vertical temperature

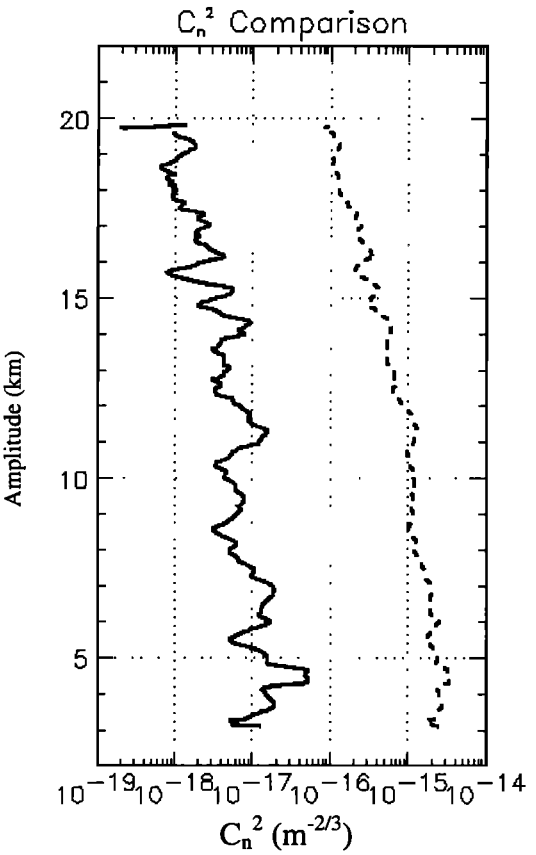

Figure 11. C_n^2 calculated from the higher-order temperature difference. Dashed curve is C_n^2 calculated from the first-order temperature difference. Solid curve is C_n^2 from the second-order temperature difference.

difference is almost indistinguishable from the results of the higher-order difference. We show this as the solid curve. This is powerful evidence that the higher-order structure functions successfully isolate the turbulent component. On basis of the published, experimentally measured values of C_n^2 [e.g., *Coulman et al.*, 1995; *Walters*, 1995; *Hocking and Mu*, 1997, and references therein] the typical values of C_n^2 range from a lower limit of ~10^{-19} $m^{-2/3}$ to an upper limit of ~10^{-14} $m^{-2/3}$. The C_n^2 values calculated here are near the lower bound.

6.3. Calculation of C_n^2 via the Fourier Power Spectrum

For isotropic turbulence in the inertial subrange we can relate C_n^2 to the one-dimensional spectrum of the passive scalar via

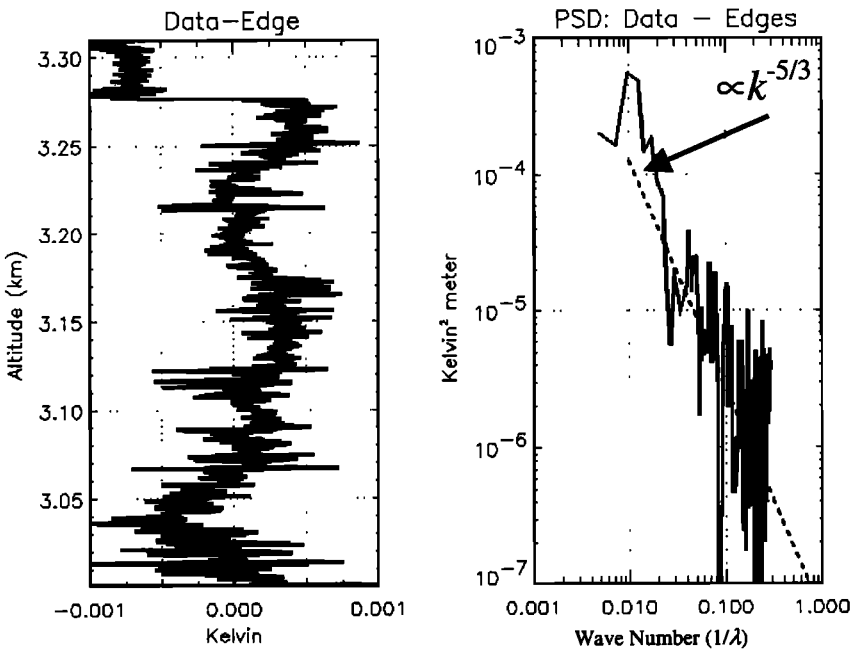

Figure 12. An example of the turbulence spectrum evaluation. (left) An example of the turbulence residual extracted from the temperature data via the edge-tracking algorithm. (right) The power spectral density (PSD) of the turbulence residual. Dashed curve has a -5/3 slope.

$$S_n(k) \approx \frac{1}{4} C_n^2 k^{-5/3}, \tag{26}$$

where S_n is the one-dimensional Fourier spectrum of the refractive index as measured by a sensor moving through the medium and k is the radian wave number corresponding to the spatial wavelength $2\pi k^{-1}$ [*Ottersten*, 1968].

We can apply (26) to the residual signal, which we believe includes the turbulent component of the data to calculate C_n^2. In detail, we first parse the turbulent data into segments 300 m in length. We then calculate the Fourier spectra of that data segment, fit a line following a –5/3 slope to the spectrum, and evaluate the spectrum at $k = 2\pi/\lambda$, where $\lambda = 50$ m, which is in the inertial subrange and is such that $S_n(k)$ is well above the noise level. We show an example of this in Figure 12. The result of the C_n^2 calculation is plotted in Figure 13 as the dashed curve. The values of C_n^2 computed from the Fourier analysis of our residual signal are similar to that derived from the higher-order vertical temperature differences (solid curve). The two profiles, in fact, match each other quite well in the troposphere; in the stratosphere, C_n^2 derived from our residual signal is usually lower than the one given by the *Walters'* [1995] method. This not only verifies the effectiveness of the edge-tracking algorithm in isolating the coherent structures in the temperature data but also confirms that turbulence does exist in the data! Note that if $S_n(k)$ had been directly calculated from the original Fourier spectrum given in Figure 7, C_n^2 would have been several orders of magnitude larger than was found with the residuals.

6.4. Turbulence Scatter

The calculated C_n^2 will give us turbulent radar backscatter with which we can compare the backscatter from Fresnel scatter and derive the radar aspect sensitivity. For radars with wavelengths from meters to centimeters, where the spatial scale $L = 2\pi k^{-1} = 0.5\lambda$ and λ is the radar wavelength, determining the backscattering will generally fall within the inertial subrange. Under this assumption, *Ottersten* [1968, 1969a, 1969b] derives a relationship of the reflectivity of a scattering volume to the one-dimensional Fourier spectra of the turbulent refractive index S_n,

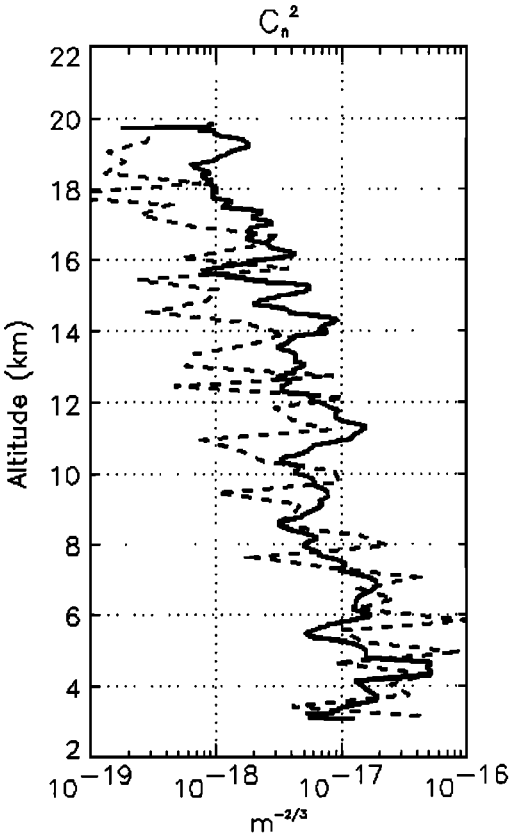

Figure 13. C_n^2 calculated from two different approaches. Solid curve is C_n^2 calculated from the higher-order temperature difference. Dashed curve is C_n^2 as determined from the Fourier spectrum of the residual signal. The two results agree very well, particularly in the tropospheric region of the atmosphere.

$$\eta(k) = (5/3)(\pi/8)k^2 S_n(k) \ [\mathrm{m}^2/\mathrm{m}^3], \qquad (27)$$

This, with (26), gives

$$\eta(\lambda) \approx 0.38 C_n^2 \lambda^{-1/3} \ [\mathrm{m}^2/\mathrm{m}^3]. \qquad (28)$$

The volume reflectivity is a measurement of reflectivity caused by a volume of scatters in contrast to the reflection coefficient ρ, a measurement of the reflection coefficient from a slab structure. Since we have already made a postulation of ρ on the basis of Fresnel scatter from the steep edges in the data set, we need to relate η to ρ in some way. Fortunately, *Röttger and La Hoz* [1990] have compared the reflected power based on ρ and the reflected power based on η and have obtained the following conversion factor,

$$\eta = \frac{4A_e}{\Delta r \lambda^2} |\rho|^2, \qquad (29)$$

where Δr is the range resolution of the radar, A_e is the effective area, and λ is the radar wavelength. We can use this to convert our η from turbulence to an effective ρ and then compare this effective ρ to the ρ we calculated from Fresnel scattering. Again, it is necessary to go through this conversion to compare the effectiveness of radar backscatter caused by two different mechanisms, one being an edge scattering mechanism while the other is a turbulent volume scattering. To perform the conversion, we have taken the parameters of the MU radar, with λ = 6.45 m, Δr = 300 m, and A_e = 8330 m^2. We use the MU radar because the MU radar and the observed balloon data are both located at midlatitudes. Furthermore, the MU radar has been used to measure the aspect sensitivity of the lower atmosphere [*Tsuda et al.*, 1997]. We plot the result as the starred curve in Figure 10 using the *Walters* [1995] value of C_n^2, which we believe to be more reliable in this case than the turbulence residuals. In this turbulence scattering calculation, to compute C_n^2 from the residuals, one needs to compute the Fourier power spectrum, a calculation that has difficulty dealing with data gaps and uneven sampling, and great care must be taken to avoid spectral leakage. Structure functions, the foundation of *Walters'* method, do not have such problems and are easily computed. The turbulent component is clearly well below the edge component for this event, which is characteristic of the aspect sensitivity of radar scatter from the atmosphere, as discussed in section 7.

7. Aspect Sensitivity Calculation

The aspect sensitivity of the radar backscatter power has been examined for the troposphere and lower stratosphere by many researchers. It has been shown that the effect is more pronounced in the more stable, lower stratosphere than in the troposphere [e.g., *Gage and Green*, 1978; *Röttger*, 1980; *Tsuda et al.*, 1986, 1997]. Since our balloon data were observed in midlatitudes, we have investigated the measured aspect sensitivity at similar locations. *Hooper and Thomas* [1995] made radar observations in Wales of the backscattered signal in the vertical direction and at zenith angles of 4.2°, 6°, 8.5°, and 12°. The radar operates at a frequency of 46.5 MHz with Δr = 150 m and A_e = 11,000 m^2. At a zenith angle of

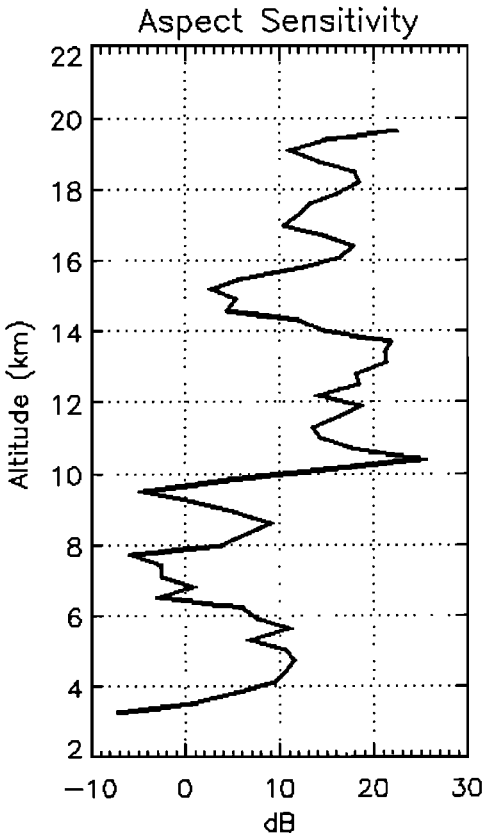

Figure 14. The predicted aspect sensitivity that the MU radar may observe from this temperature sounding. We have used the C_n^2 from the higher-order difference to calculate the equivalent reflection coefficient of isotropic turbulence. We see that the aspect sensitivity is -15 decibels in the troposphere and 25 decibels in the stratosphere.

12° the backscattered power is ~10 decibels below the vertical power at 6 km and 20 decibels less at 14 km. *Sato et al.* [1985], using the MU radar in Japan, studied the characteristics of specular echoes reflected from stratified layers in the troposphere and lower stratosphere and found similar aspect sensitivity characteristics. In a more recent measurement, *Tsuda et al.* [1997] found that radar backscatter power initially decreases as a function of zenith angle but gradually reaches a constant level between 15 and 25 decibels down at $\theta > 20°$. This constant level is interpreted as the isotropic turbulence scattering level. We use the ratio of vertical scatter power to off-vertical isotropic turbulence scatter power as our measure of aspect sensitivity.

In Figure 14 we plot the ratio of the reflected power on the basis Fresnel scattering, accounting for the measured horizontal correlation length, to the value we predicted for turbulent scatter for the MU radar as if it had been operating on the night of the balloon flight on March 5, 1995. Similar to experimental observations, the ratio of vertical Fresnel scatter power in the lower stratosphere to the isotropic component is ~15 decibels. Similarly, we find the aspect sensitivity to be ~10 decibels or less in the troposphere. We contribute aspect sensitivity < 0 to the fact that we had assumed the horizontal correlation length in the troposphere to be constant (~3 m), which is adequate for a back-of-the-envelope calculation. We suspect that the higher aspect sensitivity in the stratosphere is related to the greater stability of that part of the atmosphere.

8. Conclusion

We have analyzed a high-resolution temperature measurement of the lower atmosphere. What catches our attention are the potential temperature steps and the sharp temperature gradients observed at the edges of these steps. For a better understanding of the atmospheric dynamics, we wavelet-analyze the data and parse it into its edge and turbulence components. Wavelets seem to be a promising tool with which to study coherent structures in the atmosphere. In addition, once the coherent structures are removed, the residual signal seems to well represent the turbulent component of the atmospheric structure. The latter statement is supported by the comparison of C_n^2 found from the Fourier analysis of the residual signal and C_n^2 determined with the high-order structure function. Prediction of VHF scatter from the coherent and turbulent structures is in good agreement with observations, as are our estimates of the aspect sensitivity.

The atmospheric structures, which yield the strong scatter in the vertical direction, are similar to the so-called ramp-cliff features reported in boundary layer and temperature sheets in the troposphere and stratosphere. In our case, the steepest gradients and strongest scatter are found to have positive temperature gradients, i.e., the cliff component. The ramp portion has corresponding potential temperature gradients near zero, corresponding to the stability boundary for convective turbulence and, most likely, to a gradient Richardson number near 0.25, as may well result from a dynamic instability.

Acknowledgments. We thank D. Farley, D. Fritts, and D. Gibson-Wilde for insightful comments and discussions.

References

Alcala, C. M., and M. C. Kelley, Nonturbulent layers in polar summer mesosphere, 2, Application of wavelet analysis to VHF scattering, *Radio Sci.*, this issue.

Alcala, C. M., M. C. Kelley, and J. Ulwick, Nonturbulent layers in polar summer mesosphere, 1, Detection of sharp gradients using wavelet analysis, *Radio Sci.*, this issue.

Antonia, R. A., and J. D. Atkinson, A ramp model for turbulent temperature fluctuations, *Phys. Fluids*, *19*, 1273-1278, 1976.

Antonia, R. A., A. J. Chambers, C. A. Friehe, and C. Q. Van Atta, Temperature ramps in the atmospheric surface layers, *J. Atmos. Sci.*, *36*, 99-108, 1977.

Balsley, B. B., The MST technique-A brief review, *J. Atmos. Terr. Phys.*, *43*, 495-509, 1981.

Balsley, B. B., and K. S. Gage, The MST radar technique: Potential for middle atmospheric studies, *Pure Appl. Geophys.*, *118*, 452-493, 1980.

Barat, J., Some characteristics of clear-air turbulence in the middle atmosphere, *J. Atmos. Sci.*, *39*, 2553-2565, 1982.

Barat, J., and F. Bertin, Simultaneous measurement of temperature and velocity fluctuations within clear-air turbulence layers: Analysis of the estimate of dissipation rate by remote sensing techniques, *J. Atmos. Sci.*, *41*, 1613-1619, 1984.

Bean, B. R., and E. J. Dutton, *Radio Meteorology, U.S. Natl. Bur. Stand., Monogr. 92, Supt. Docs.*, U.S. Govt. Print. Off., Washington, D. C., 1966.

Bertin, F., J. Barat, and R. Wilson, Energy dissipation rates, eddy diffusivity, and the Prandtl number: An in situ experimental approach and its consequences on radar estimates of turbulent parameters, *Radio Sci.*, *32*, 791-804, 1997.

Booker, H. G., and W. E. Gordon, A theory of radio scattering in the troposphere, *Proc. IEEE*, *38*, 401-412, 1950.

Briggs, B. H., and R. A. Vincent, Some theoretical considerations on remote probing of weakly scattering irregularities, *Aust. J. Phys.*, *26*, 805-814, 1973.

Bufton, J. L., P. O. Minott, M. W. Fitzmaurice, and P. Titterton, Measurements of turbulence profiles in the troposphere, *J. Opt. Soc. Am.*, *62*, 1068-1070, 1972.

Coulman, C. E., J. Vernin, and A. Fuchs, Optical seeing-mechanism of formation of thin turbulent laminae in the atmosphere, *Appl. Opt.*, *34*, 5461-5474, 1995.

Dalaudier, F., M. Crochet, and C. Sidi, Direct comparison between in situ and radar measurements of temperature fluctuation spectra: A puzzling result, *Radio Sci.*, *24*, 311- 324, 1989.

Dalaudier, F., C. Sidi, and M. Crochet, Direct evidence of 'sheets' in the atmospheric temperature field, *J. Atmos. Sci.*, *51*, 237-248, 1994.

Daubechies, I., *Ten Lectures on Wavelets*, Soc. for Ind. and Appl. Math., Philadelphia, Pa., 1992.

Doviak, R. J., and D. S. Zrnic, Reflection and scatter formula for anisotropically turbulent air, *Radio Sci.*, *19*, 325-336, 1984.

Gage, K. S., and J. L. Green, Evidence for specular reflection from monostatic VHF radar observation of the stratosphere, *Radio Sci.*, *13*, 991-1001, 1978.

Gage, K. S., J. L. Green, and T. E. Van Zandt, Use of Doppler radar for the measurement of atmospheric turbulence parameters from the intensity of clear air echoes, *Radio Sci.*, *15*, 407-416, 1980.

Gibson-Wilde, D., J. Werne, D. Fritts, and R. Hill, Direct numerical simulation of VHF radar measurements of turbulence in the mesosphere, *Radio Sci.*, *35*, 783-798, 2000.

Green, J. L., and K. S. Gage, Observations of stable layers in the troposphere and stratosphere using VHF radar, *Radio Sci.*, *15*, 395-405, 1980.

Hagelberg, C. R., and N. K. Gamage, Applications of structure preserving wavelet decompositions to intermittent turbulence, a case study, *Wavelets in Geophysics*, edited by E. Foufoula-Georgiou and P. Kumar, pp. 45-80, Academic, San Diego, Calif., 1994.

Hocking, W. K., Radar studies of small-scale structure in the upper and middle atmosphere and lower ionosphere, *Adv. Space Res.*, *7*, 327-338, 1987.

Hocking, W. K., Seasonal variation of turbulence intensities in the upper mesosphere and lower thermosphere measured by radar techniques, in *Handbook for MAP*, *27*, pp. 427-438, SCOSTEP Sec., Univ. of Ill., Urbana, 1989.

Hocking, W. K., and P. K. L. Mu, Upper and middle tropospheric kinetic energy dissipation rates from measurements of C_n^2–Review of theories, in situ investigations, and experimental studies using the Buckland Park atmospheric radar in Australia, *J. Atmos. Sol. Terr. Phys.*, *99*, 1779-1803, 1997.

Hocking, W. K., R. Rüster, and P. Czechowsky, Absolute reflectivities and aspect sensitivities of VHF radio waves scatterers measured with the SOUSY radar, *J. Atmos. Terr. Phys.*, *48*, 131-144, 1986.

Hocking, W. K., S. Fukao, T. Tsuda, M. Yamamoto, T. Sato, and S. Kato, Aspect sensitivity of stratospheric VHF radio waves scatters, particularly above 15 km altitude, *Radio Sci.*, *25*, 613-627, 1990.

Holton, J., *An Introduction to Dynamic Meteorology*, Academic, San Diego, Calif., 1992.

Hooper, D., and L. Thomas, Aspect sensitivity of VHF scatters in the troposphere and stratosphere from comparisons of powers in off vertical beams, *J. Atmos. Sol. Terr. Phys.*, *57*, 655-663. 1995.

Kaimal, J. C., and J. A. Businger, Case studies of a con-

vective plume and dust devil, *J. Appl. Meteorol.*, *9*, 612-620, 1970.

Kumar, P. and E. Foufoula-Georgiou, Wavelet analysis in geophysics: An introduction, *Wavelets in Geophysics*, edited by E. Foufoula-Georgiou and P. Kumar, pp. 1-44, Academic, San Diego, Calif., 1994.

Mallat, S., and S. Zhong, Characterization of signals from multiscale edges, *IEEE Trans. Pattern Anal. Mach. Intell.*, *14*, 710-732, 1992.

Ottersten, H., Theoretical aspects of CAT detection by radar, paper presented at Proc. 13th Radar Meteorology Conference, Am. Meteorol. Soc., Montreal, Que., Canada, 1968.

Ottersten, H., Radar backscattering from turbulent clear atmosphere, *Radio Sci.*, *4*, 1251-1255, 1969a.

Ottersten, H., Atmospheric structure and radar backscattering in clear air, *Radio Sci.*, *4*, 1179-1193, 1969b.

Panofsky, H.A., The structure constant for the index of refraction in relation to the gradient of index of refraction in the surface layer, *J. Geophys. Res.*, *73*, 6047-6049, 1968.

Röttger, J., Reflection and scattering of VHF signals from atmospheric refractivity structures, *Radio Sci.*, *15*, 259-276, 1980.

Röttger, J., and C. La Hoz, Characteristics of polar mesosphere summer echoes (PMSE) observed with the EISCAT 224 MHz radar and possible explanations of their origin, *J. Atmos. Terr. Phys.*, *52*, 893-906, 1990.

Saito, N., Simultaneous noise suppression and signal compression using a library of orthonormal bases and the minimum description length criterion, *Wavelets in Geophysics*, edited by E. Foufoula-Georgiou, E. and P. Kumar, pp. 299-324, Academic, San Diego, Calif., 1994.

Sato, T., T. Tsuda, S. Kato, S. Morimoto, S. Fukao, and I. Kimura, High-resolution MST observations of turbulence by using the MU radar, *Radio Sci.*, *20*, 1452-1460, 1985.

Tatarskii, V. I., *Wave Propagation in a Turbulent Medium*, translated from Russian by R. A. Silverman, McGraw-Hill, New York: 1961.

Taylor, R. J., Thermal structures in the lowest layers of the atmosphere, *Aust. J. Phys.*, *11*, 168-176, 1958.

Torrence, C., and G. P. Compo, A practical guide to wavelet analysis, *Bull. Am. Meteorol. Soc.*, *79*, 61-78, 1998.

Tsuda, T., T. Sato, K. Hirose, S. Fukao, and S. Kato, MU radar observations of the aspect sensitivity of the backscattered VHF echo power in the troposphere and lower stratosphere, *Radio Sci.*, *21*, 971-980, 1986.

Tsuda, T., T. E. Van Zandt, and H. Saito, Zenith-angle dependence of VHF specular reflection echoes in the lower atmosphere, *J. Atmos. Sol. Terr. Phys.*, *59*, 761-775, 1997.

Van Atta, C. W., Effect of coherent structures on structure functions of temperature atmospheric boundary layer, *Arch. of Mech.*, *29*(1), 161-171, 1977.

Wait, J., *Electromagnetic Waves in Stratified Media*, Pergamon, New York, 1962.

Walters, D. L., Measurements of optical turbulence with higher order structure functions, *Appl. Opt.*, *34*, 1591-1597, 1995.

Werne J., and D. Fritts, Stratified shear turbulence: Evolution and statistics, *Geophys Res. Lett.*, *26*, 439-442, 1999.

Yaglom, A. M., *Correlation Theory of Stationary and Related Random Functions I and II*, Springer-Verlag, New York, 1987.

C. Y. Chen and M. C. Kelley, School of Electrical and Computer Engineering, Cornell University, Ithaca, NY 14853. (chuck@ece.cornell.edu; mikek@ece.cornell.edu)

D. L. Walters, Department of Physics, Naval Postgraduate School, Monterey, CA 93943. (walters@nps.navy.mil)

(Received April 5, 2000; revised February 9, 2001; accepted February 12, 2001.)